APL Photonics

All-dielectric rod antenna array for terahertz communications

Cite as: APL Photonics 3, 051707 (2018); https://doi.org/10.1063/1.5023787
Submitted: 28 January 2018 . Accepted: 03 April 2018 . Published Online: 20 April 2018

Withawat Withayachumnankul, Ryoumei Yamada, Masayuki Fujita, and Tadao Nagatsuma

APL PHOTONICS **3**, 051707 (2018)

All-dielectric rod antenna array for terahertz communications

Withawat Withayachumnankul,[1,a] Ryoumei Yamada,[2] Masayuki Fujita,[2,b] and Tadao Nagatsuma[2]
[1]*School of Electrical and Electronic Engineering, The University of Adelaide, Adelaide, SA 5005, Australia*
[2]*Graduate School of Engineering Science, Osaka University, 1-3 Machikaneyama, Toyonaka, Osaka 560-8531, Japan*

(Received 28 January 2018; accepted 3 April 2018; published online 20 April 2018)

The terahertz band holds a potential for point-to-point short-range wireless communications at sub-terabit speed. To realize this potential, supporting antennas must have a wide bandwidth to sustain high data rate and must have high gain and low dissipation to compensate for the free space path loss that scales quadratically with frequency. Here we propose an all-dielectric rod antenna array with high radiation efficiency, high gain, and wide bandwidth. The proposed array is integral to a low-loss photonic crystal waveguide platform, and intrinsic silicon is the only constituent material for both the antenna and the feed to maintain the simplicity, compactness, and efficiency. Effective medium theory plays a key role in the antenna performance and integrability. An experimental validation with continuous-wave terahertz electronic systems confirms the minimum gain of 20 dBi across 315–390 GHz. A demonstration shows that a pair of such identical rod array antennas can handle bit-error-free transmission at the speed up to 10 Gbit/s. Further development of this antenna will build critical components for future terahertz communication systems.
https://doi.org/10.1063/1.5023787

I. INTRODUCTION

Research activities in terahertz communications have become intensive in recent years.[1] This is in response to the congestion at lower microwave and millimeter-wave frequency bands due to the exponential growth of wireless devices and associated high-quality multimedia. According to Shannon theorem, moving to higher frequencies offers wider bandwidth and thus higher channel capacities. Conceptually, a single terahertz band within an atmospheric transmission window can carry over 100-Gbit/s wireless data across a few hundreds of metres.[1] Indeed, terahertz links cannot replace existing mobile communication channels because of the stringent alignment of a transmitter-receiver pair at higher frequencies. However, such high-capacity links are in demand to serve between fixed base stations of future mobile networks, within large data centres, at data kiosks, and for intra-/inter-chip communications. One major challenge toward terahertz communications lies in radiating antennas that must have high directivity to compensate free-space path loss, high efficiency to preserve precious terahertz power, and wide bandwidth to support large channel capacity.

At terahertz frequencies, metals can no longer be considered as quasi-perfect electric conductors. Ohmic loss is non-negligible, particularly when oscillations of surface currents are involved, as in resonant metallic antennas. Despite that, nearly all existing terahertz antennas were made of metals.[2] Additionally, these antennas typically co-locate and cooperate with either electronic[3,4] or

[a]Electronic mail: withawat@adelaide.edu.au
[b]Electronic mail: fujita@ee.es.osaka-u.ac.jp

photonic[5] sources, and as such the designability of the antennas and the functionality of the platform are limited. For terahertz communication demonstrations, high-gain radiation is supported by augmenting parabolic reflectors, lenses, or horns.[6–8] While the bandwidth, gain, and efficiency of these components are attractive, their size and shape greatly limit the integrability. Recent studies employed compact dielectric resonator antennas to mitigate or eliminate Ohmic loss in metallic antennas.[9–11] However, the gain and bandwidth were relatively limited. As an alternative, non-resonant planar travelling-wave antennas promise integrability, wideband performance, and low dissipation.

In principle, a single tapered dielectric rod antenna[12,13] can be employed to achieve high-gain radiation. This type of antenna gradually leaks a guided mode into free space to form a large effective aperture. Such a rod antenna possesses broad bandwidth, high gain, low insertion loss, and frequency-independent radiation pattern. The feed for a rod antenna can be a dielectric waveguide.[14,15] So far, all terahertz-range implementations were in the form of a single rod fed by a horn antenna or a local source.[16–18] Achieving high radiation gain can be accomplished by extending the rod length. However, this method is restricted by the fragility of the long tapering. To put this into perspective, a numerical estimation suggests a rod length of over 50 mm or 55 wavelengths to attain the gain of 20 dBi at 330 GHz (see the supplementary material). An alternative means to attaining high gain is to employ an array of multiple rod antennas to increase an effective aperture size. Such arrays were implemented for millimeter waves,[19–21] but the feed networks were complicated and not scalable to the terahertz range. Additionally, those rod antenna arrays were with limited density and expandability due to a large feed extent.

In this article, we present an array of dielectric rod antennas to support wireless communications at terahertz frequencies between 300 and 400 GHz. This antenna array is designed to work in conjunction with a photonic crystal waveguide platform. High radiation gain can be realized from a number of rod antennas, together forming a large effective aperture. This array is fed by a flaring dielectric waveguide to reduce the complexity of the feed network and to accommodate the array density and scalability. The feed length can be greatly shortened by the use of an effective medium to correct the wavefronts across the aperture. The entire structure, comprising the antenna array and the photonic crystal platform, can be built all at once on a single dielectric material. This integrated structure simplifies the fabrication process and fully complies with the restrictions imposed by micro-fabrication technology. Since both the feeding photonic crystal waveguide and antenna are all-dielectric, Ohmic loss associated with metals is entirely eliminated. Importantly, the design consolidates knowledge from both the microwave and optics domains with the involvement of dielectric rod antenna, photonic crystal waveguide, and effective medium.

II. DESIGN PRINCIPLE

A. Overview

As shown in Fig. 1, the proposed antenna is established as a part of the free-standing photonic crystal platform. The structure comprises a photonic crystal waveguide, a planar horn or flaring section, an effective medium, and an array of tapered dielectric rod antennas. These planar components work together to couple a guided mode with free-space radiation. All the components are defined into a 200-μm thick silicon slab in the form of air through-holes. This silicon is intrinsic and float-zone and thus exhibits very small dissipation loss[22] in the terahertz range, i.e., $\tan\delta \approx 0.000\,02$ at 1 THz. It suggests that the antenna efficiency is close to 100%. The bulk refractive index of silicon is around 3.418 in this frequency range.[22] A high contrast between the refractive indices of bulk silicon and free space results in strong wave confinement and overall compact structure. Furthermore, the contrast yields an effective medium with a potentially large variation in the effective index, which can accommodate a wide range of artificial dielectric components. In this section, we discuss each component in Fig. 1 in detail. All the simulations are carried out by using CST Microwave Studio.

The feed employs an existing low-loss photonic crystal waveguide that supports a dominant transverse-electric (TE) mode with an electric field in-plane and a magnetic field out-of-plane.[23] This TE mode is present between 315 and 336 GHz, within which the waves are tightly confined in plane by the photonic-bandgap effect and out of plane by the total-internal reflection. The attenuation in this

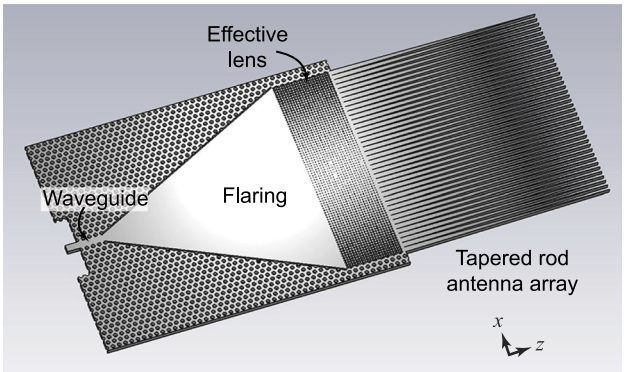

FIG. 1. Render of optimal dielectric rod antenna array and feed. Visible in this image from left to right are the photonic crystal waveguide, flaring section, effective medium, and tapered rod array. All the dimensions are given in the supplementary material.

waveguide is less than 0.1 dB/cm. In order to feed an array of dielectric rod antennas, this waveguide flares into a planar dielectric waveguide that supports a TE_0 mode with an electric field in the x direction. The photonic crystal remains alongside the flaring section to prohibit in-plane leakage.[24] The mode conversion between the photonic crystal waveguide and the planar dielectric waveguide is with negligible insertion loss. It should be noted that the two TE modes are distinctive due to different naming conventions. By definition, only the former has an electric-field component in the propagation direction. For the planar dielectric waveguide, all modes are slow-wave with evanescent field out of plane.

This flared-out planar dielectric waveguide feeds an array of identical dielectric rod antennas. Each rod antenna loosely operates in its HE_{11} mode and is spaced apart from an adjacent one by 200 μm. The rods are tapered such that the guided mode gradually leaks into free space in both transversal directions. Given the spacing of the rod array, grating lobes can be expected around 1.5 THz, well above the frequency range of interest. Since this feed scheme entails no sophisticated power dividers, the rod antennas can be closely packed and readily expandable. Typically, a larger aperture size would translate directly to a larger antenna gain.[25] However, the validity of this relation is limited to some extent. As the aperture grows larger, in-plane cylindrical waves become obvious in the flaring section. In other words, a wave travelling from the photonic crystal waveguide to each dielectric rod antenna acquires a distinctive phase delay due to different path lengths. This leads to a diverging beam in free space. As a consequence, the achievable gain saturates at around 12–15 dBi for a given tapered rod length. A possible solution is to increase the ratio between the length and the width of the flaring section to reduce the difference in the path lengths. However, the approach obviously undermines the compactness of the feed.

In principle, a lens should be inserted between the flaring section and the rod array to equalize the phase delay for different paths, i.e., stronger delay on-axis and weaker delay for longer diverging paths off-axis. Based on this requirement, we adopt effective medium theory to perform this lensing function without introducing additional materials or fabrication steps. The framework of an effective medium has been realized to create different devices, as, for example, a gradient-index lens for free-space terahertz waves,[26] a planar Luneburg lens,[27] and even an optical cloak.[28] For our work, a two-dimensional array of subwavelength cylindrical air thru-holes is created into the planar dielectric waveguide, and the effective modal index of this waveguide can be controlled via the hole density. Thus, spatial phase variation across the aperture can be produced. Reflection at the lens-waveguide interfaces should be minimal to avoid additional insertion losses and gain variation with frequency.

B. Effective medium in dielectric waveguide

First, we consider the effective permittivity ϵ_{eff} of bulk silicon perforated by an array of cylindrical air holes. For the propagation mode under consideration, the electric-field polarization is always perpendicular to the axis of these air holes. In this case, the 2D Maxwell-Garnett approximation

establishes that[29]

$$\epsilon_{\text{eff}} = n_{\text{eff}}^2 = \epsilon_{\text{si}} \frac{(\epsilon_0 + \epsilon_{\text{si}}) + (\epsilon_0 - \epsilon_{\text{si}})\zeta_d}{(\epsilon_0 + \epsilon_{\text{si}}) - (\epsilon_0 - \epsilon_{\text{si}})\zeta_d}, \tag{1}$$

where ζ_d is a fill factor, $\epsilon_0 = 1$ is the relative permittivity of free space, and $\epsilon_{si} = n_{si}^2 = 11.68$ is the relative permittivity of silicon, which is constant in the terahertz range. For a square lattice of air holes, the fill factor ζ_d can be calculated from $\pi d^2/(4a^2)$, where d is the diameter of an air hole and a is the lattice constant, i.e., the distance between the centers of adjacent holes. This approximation is valid when the hole array is in the subwavelength regime, i.e., the lattice constant a is much smaller than the shortest wavelength of guided waves. Under this assumption, diffraction and bandgap effects do not play a role. It is noteworthy that this effective medium inherits its non-dispersion from bulk silicon.

Then, we consider the relevant mode of propagation inside the planar silicon waveguide, and how this mode is affected by the presence of subwavelength air holes. Between 300 and 400 GHz, the dielectric waveguide made of a 200-μm thick silicon slab can support two TE modes, namely, TE_0 and TE_1, the former of which has no cutoff frequency and the latter has its cutoff at 241 GHz. However, only the fundamental mode is of interest here since the TE_1 mode is asymmetric and thus cannot be excited by the photonic crystal waveguide. The propagation constant β of TE modes in this free-standing planar dielectric waveguide, as shown in the inset of Fig. 2, can be expressed in the transcendental form as[30]

$$\tan^2\left\{\frac{t}{2}\sqrt{(n_{\text{eff}}k_0)^2 - \beta^2} - \frac{m\pi}{2}\right\} = \frac{\beta^2 - k_0^2}{(n_{\text{eff}}k_0)^2 - \beta^2}, \tag{2}$$

where k_0 is the free-space wavenumber, $t = 200$ μm is the waveguide thickness, $m = 0$ is the fundamental propagation mode, and n_{eff} is the effective refractive index of the constituent dielectric materials. For bulk silicon, n_{eff} equals 3.418, while n_{eff} for perforated silicon can be obtained from Eq. (1). Based on Eq. (2), at 400 GHz, the wavelength of the TE_0 mode inside an unperforated silicon slab equals 240 μm. Thus, the lattice constant of air holes must be less than 120 μm to maintain the validity of effective medium approximation. In the following designs, the lattice constant is 100 μm or less. For this choice of lattice constant, the first bandgap appears at around 470 GHz, well above the frequency range of interest.

Figure 2(a) shows how the dispersion relation of the planar waveguide changes with the diameter of air holes with a lattice constant of 100 μm. It can be seen that the guided mode remains below the light line with no free-space coupling. In addition, Fig. 2(b) shows the corresponding effective modal

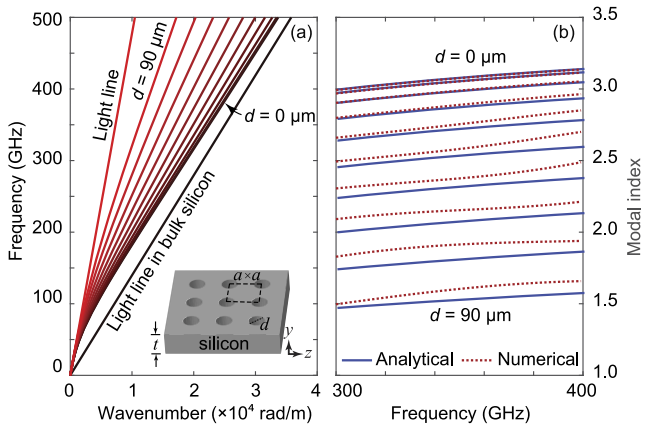

FIG. 2. Effect of the subwavelength hole array on the guided mode. (a) Dispersion relation for the TE_0 mode inside the planar dielectric waveguide. The lattice constant a of the hole array is set to 100 μm, while the hole diameter d varies between 0 μm and 90 μm with a step size of 10 μm. The results are obtained by using Eq. (2) with an assumption of homogeneous material. This assumption excludes the bandgap effect that occurs around 470 GHz due to the periodicity of the hole array. (Inset) A planar dielectric waveguide in free space with a square lattice of air holes. (b) Corresponding effective modal indices $n_{\text{wg}} = \beta/k_0$ for the TE_0 mode. The analytical results are from Eq. (2), while the numerical results are from CST Microwave Studio.

indices, $n_{wg} = \beta/k_0$, which will be used in designing the effective medium for phase correction. It is clear that the modal index decreases with an increase in the hole size. In addition, this modal index is dispersive as a consequence of the guided mode, i.e., higher frequency components experience slightly larger effective refractive index due to tighter field confinement. However, within the frequency range of interest between 300 and 400 GHz, the dispersion is moderate, and the following calculations assume frequency-independent modal indices taken at 330 GHz. Figure 2(b) also provides a comparison with numerical results that show general agreement. The deviation between the analytical and numerical results, particularly for large hole diameters, is because of the Fabry-Perot effect inside the simulated waveguide. The reflections arise since the wave impedance of the ports matches that of the mode in the silicon slab, but not in the effective medium.

C. Design of effective lens

An effective lens can be designed based on the relation between the hole diameter and the effective modal index. The phase distribution of this lens necessary to compensate the phase difference due to wave propagation in the flaring section is given as

$$\phi_{\text{lens}}(x) = n_{\text{wg},d=0} k_0 (\sqrt{F^2 + x^2} - F) + \phi_0 \,, \tag{3}$$

where $n_{\text{wg},d=0}$ is the modal index of the dielectric waveguide without a hole array, F is the focal length, and ϕ_0 is an arbitrary phase constant. It is noteworthy that engineering phase convention is adopted throughout. Equation (3) assumes a fixed modal index over the flaring section for simplicity. Practically, this modal index varies along the propagation or z axis due to the evolution of the guided mode, as discussed in Sec. II A. The focal length F can be adjusted around the flare length to compensate this spatial modal index variation. The phase offset ϕ_0 enforces negative phase values associated with phase retardation inside the lens. Equation (3) implies that this lens induces strongest phase delay in the center where $x = 0$.

On the other hand, the phase response available from the effective medium is given as

$$\phi_{\text{avail}} = -n_{\text{wg},d} k_0 l \,, \tag{4}$$

where $n_{\text{wg},d}$ is the modal index of the dielectric waveguide loaded with an array of air holes with a diameter d and l is the length of this effective lens along the z axis. This phase response can be tailored to match the phase requirement in Eq. (3) by varying either the modal index $n_{\text{wg},d}$ or the length l. The latter option implies a constant index contrast across the aperture, and thus a considerable Fabry-Perot effect. Thus, we opt for the former option to fix the length l but vary the hole diameter d along the x direction, as illustrated in Fig. 3. The smallest hole diameter d_{min} locates around $x = 0$ to induce a strongest delay, while the largest hole diameter d_{max} locates on the edges. The physical length l

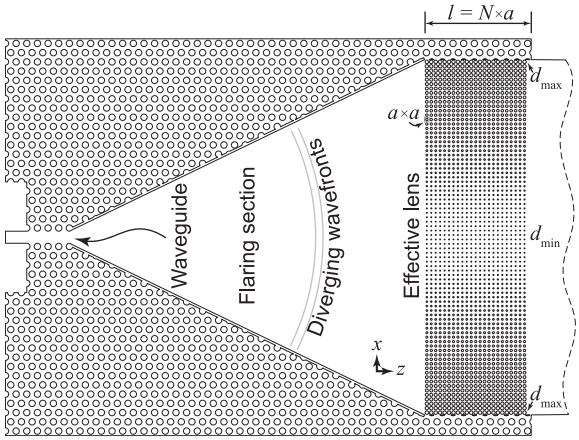

FIG. 3. Effective lens for wavefront correction. Waves emerging from the photonic crystal waveguide diverge as they propagate through the flaring section. These diverging waves can be collimated by using the effective lens made of an array of cylindrical air holes.

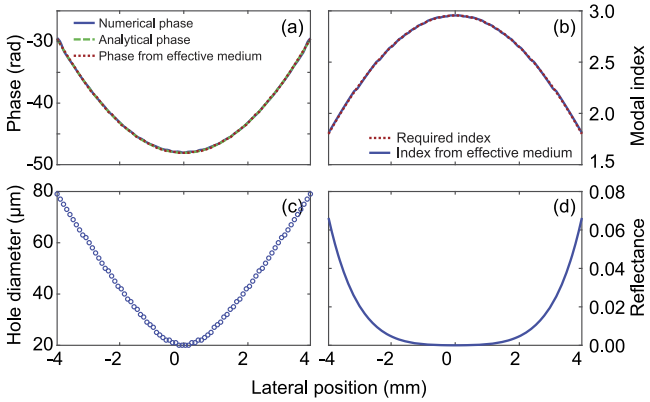

FIG. 4. Effective lens design for an optimal rod antenna array. (a) Phase profiles for the lens at 330 GHz. The analytical phase profile is obtained from Eq. (3), while the numerical phase is obtained from CST Microwave Studio across the flare end. The three curves overlap nearly completely. (b) Required modal indices calculated from Eq. (7), and modal indices available from the effective medium. (c) Corresponding hole diameters rounded to the nearest integers. (d) Reflectance at the lens-waveguide interface. This reflectance is calculated from $[n_{\mathrm{wg},d=0} - n_{\mathrm{wg},d}(x)]^2/[n_{\mathrm{wg},d=0} + n_{\mathrm{wg},d}(x)]^2$.

of this effective lens can be determined from these two hole sizes—$d_{\min}$ limited by the fabrication and $d_{\max}$ limited by the acceptable impedance mismatch with the solid dielectric waveguide. The maximum phase difference available from the two hole extrema must satisfy the maximum phase difference required by Eq. (3). Thus,

$$l = \frac{n_{\mathrm{wg},d=0}k_0(\sqrt{F^2 + x_{\max}^2} - F)}{(n_{\mathrm{wg},d_{\min}} - n_{\mathrm{wg},d_{\max}})k_0}\,. \tag{5}$$

The number of air holes along the z axis thus equals $N = l/a$, rounded to the nearest integer. The phase constant ϕ_0 in Eq. (3) must be equal to the phase accumulation along the z axis at $x = 0$, or

$$\phi_0 = -n_{\mathrm{wg},d_{\min}}k_0Na\,. \tag{6}$$

Finally, the required modal index as a function of the position x can be calculated by equating Eqs. (3) and (4),

$$n_{\mathrm{wg},d}(x) = -\frac{\phi_{\mathrm{lens}}(x)}{k_0Na}\,, \tag{7}$$

and the corresponding hole diameter at each discrete x location can be found from the relation discussed in Sec. II B. Notably, provided that the guided mode is approximately nondispersive, this phase correction approach works in broadband due to the true time delay of the effective lens. Figure 4(a) shows that the phase profile available from the effective medium can track well with the required phase profile, despite the discretization of hole diameters in a 1-μm step. In Figs. 4(b) and 4(c), the modal index profile, together with the corresponding hole diameter profile, suggests a strongest delay and a minimal index contrast at $x = 0$. This configuration results in negligible reflection around the central axis of the lens, as shown in Fig. 4(d).

III. ANTENNA CHARACTERISTICS

The optimal rod antenna array, including the effective lens and the waveguide feed, is fabricated at once by deep reactive-ion etching. This process forms vertical air holes and gaps through a silicon wafer of 200 μm thick. Figure 5(a) shows one fabricated sample. All the components are precisely developed. Particularly, the smallest and largest holes with diameters of 20 μm and 144 μm can be co-fabricated in a single run. The photonic crystal waveguide, excluding the flaring part, extends to 8.2 mm for handling purposes. The tapered dielectric waveguide of 3.0 mm long on the opposite end of the antenna can insert into and couple with a WR-3 hollow rectangular waveguide, which is the output port of the measurement setup. Through this tapered waveguide, the dominant TE_{10}

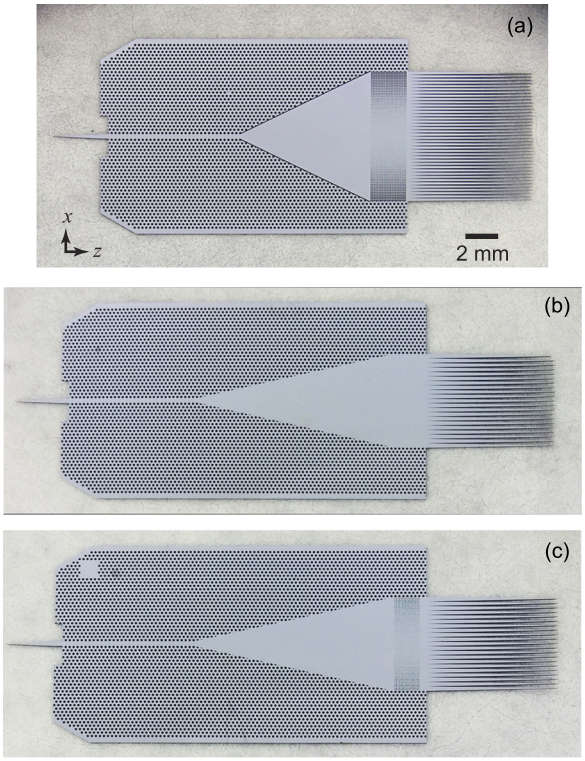

FIG. 5. Fabricated antenna arrays. (a) Optimal antenna array with an aperture width of 8 mm and a rod length of 8 mm. [(b) and (c)] Nonoptimal antenna arrays without and with effective lens for comparison. The aperture width is 5.7 mm and the rod length is 8 mm. For all antennas, the sharp tail on the left couples with a hollow rectangular waveguide of the measurement system. The images are with the same scale, but subject to different camera perspectives. The dimensions of all antenna arrays are available in the supplementary material.

mode in the rectangular waveguide gradually converts to the fundamental mode inside the photonic crystal waveguide with less than 0.2 dB insertion loss, i.e., 95.5% coupling efficiency, across the spectral band of interest (see the supplementary material).[23] Shown in Figs. 5(b) and 5(c) are other two nonoptimal antenna arrays to observe the performance of the effective lens.

The fabricated antenna arrays are characterized for their frequency-dependent gains and radiation patterns in the *E*- and *H*-planes, i.e., *xz*- and *yz*-planes, respectively. A diagram for the measurement setup is illustrated in Fig. 6. The signal generator delivers a continuous wave that is tuned around 40 GHz. This signal is directly fed into a 9× multiplier. The resulting terahertz signal ranging between 300 and 390 GHz excites the antenna under test. A WR-3 diagonal horn antenna is used at the receiver side instead of a standard conical horn antenna to reduce standing waves in free space. The transmitting and receiving antennas are separated by 300 mm. Connected to the receiving horn

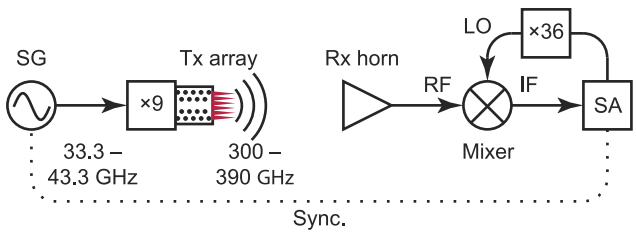

FIG. 6. Measurement system based on terahertz electronics. This system is used for the gain and radiation-pattern measurements for all antenna designs. SG: signal generator, SA: spectrum analyzer, Tx: transmitter, Rx: receiver, LO: local oscillator, RF: radio (terahertz) frequency, and IF: intermediate (microwave) frequency.

antenna, the mixer with a built-in 36× multiplier works together with the spectrum analyzer to down-convert the received terahertz signal to a microwave signal. Absorbers are placed around the antenna pair to minimize reflections. The gain of the antenna under test is calibrated with a reference standard conical horn antenna. The radiation pattern measurement is carried out with an automated system at an angular step size of 1°. Waveguide twists are employed to access the orthogonal plane for the radiation pattern measurement.

A. Comparison of antenna gain

This section presents a comparative study on the radiation gains of the three antennas, including the optimal array in Fig. 5(a) and the nonoptimal arrays without and with effective lens in Figs. 5(b) and 5(c). The effective lens for the nonoptimal rod array has a linear variation in the hole diameters, and thus the phase distribution approximates Eq. (3). In addition, the aperture width for the nonoptimal arrays is 5.7 mm, succeeded by the optimal one of 8.0 mm. Figure 7 shows the gain profiles obtained from the measurement and simulation with general agreement. Some discrepancies are caused by nonideal alignment, spurious reflections, and higher-order modes in the rectangular waveguide. All the results account for the insertion loss in the 8-mm photonic crystal waveguide. Thus, all the antennas exhibit a lower cutoff at around 315 GHz due to the absence of guided modes in the waveguide below this frequency.[23] The noise floor yields the artificial gain level in the measurement around 300 GHz. Good matching between the antennas and the feed is evident from the simulated return loss that is higher than 10 dB within the frequency band of interest.

Among the three designs, the nonoptimal rod antenna array with no lensing shows the lowest performance with the gain varying strongly around 10 dBi. Without phase correction, diverging waves are incident on the tapered rod array at oblique angles. This results in strong interference in the forward direction and thus gain variation as a function of frequency. Interestingly, the maximum gain for this antenna is roughly the same level as that obtained from a single rod antenna with the same rod length of 8 mm (see the supplementary material). Once the effective lens is incorporated, the maximum gain of this nonoptimal design is significantly improved from about 13 dBi to 19 dBi. A dip can be observed around 340–360 GHz due to the lens performance. Based on the rigorous design discussed in Sec. II, the optimal antenna array can achieve the gain of 22 dBi at maximum, and roughly above 20 dBi across 315–390 GHz. The lower range is limited by the cutoff of the photonic crystal waveguide, while the upper range is limited by the measurement setup. Thus, the 3-dB gain bandwidth is at least 21%. The measurable gain performance of the optimal design is close to that of a standard conical horn antenna, marked at around 22 dBi.

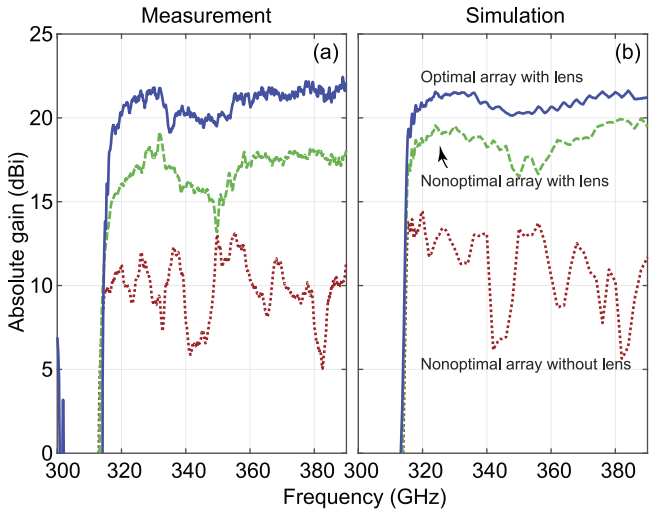

FIG. 7. Absolute-gain profiles for different antennas from measurement (a) and simulation (b). These profiles account for the insertion loss of the feeding photonic crystal waveguide of 8.2 mm.

B. Near-field and far-field characteristics of optimal antenna

This section considers only the optimal design with an emphasis on its near- and far-field characteristics. Figure 8 shows numerically resolved field distributions inside the antennas without and with the effective lens. As evident from both the amplitude and phase distributions in Figs. 8(a) and 8(c), the wave emerging from the photonic crystal waveguide evolves into a cylindrical wave inside the flare. This cylindrical wave continues to diverge in free space. Additionally, strong interference can be observed because the wave excites the rod array at oblique angles. The presence of the effective lens in Figs. 8(b) and 8(d) clearly equalizes the phase front and collimates the radiated beam. In this case, the interference is minimal since all the dielectric rod antennas operate in their intended mode. No diffraction is imposed by this effective lens due to the subwavelength packing of hole arrays. In addition, reflections inside the lens are not observable, as the majority of energy concentrates around the propagation axis, where the index mismatch is minimal. A comparison of phase profiles across the aperture in Fig. 8(e) confirms that the effective lens reduces the aperture phase difference from about 15 rad or 2.4λ to merely 1 rad or 0.16λ.

The near-field characteristics of those antennas translate to the far-field radiation patterns in Fig. 9. Two different frequencies at 330 and 360 GHz illustrate the beam stability across the bandwidth of interest. As can be seen in Figs. 9(a)–9(d), the optimal antenna without the effective lens exhibits non-directional radiation patterns. Strong destructive interference diminishes the radiation toward the endfire at 0°, and thus there is no clearly defined main lobe. Sidelobes can be observed both in the E- and H-planes. In Figs. 9(e)–9(h), the effective lens plays a central role for this rod antenna array to attain the beam quality. For this antenna, the main lobe resembles a fan beam with angular beam widths in the E- and H-planes of 6° and 32°, respectively. A wider beam in the H-plane is due to the limited aperture size out of plane. For a comparison, a standard horn antenna with a similar gain has

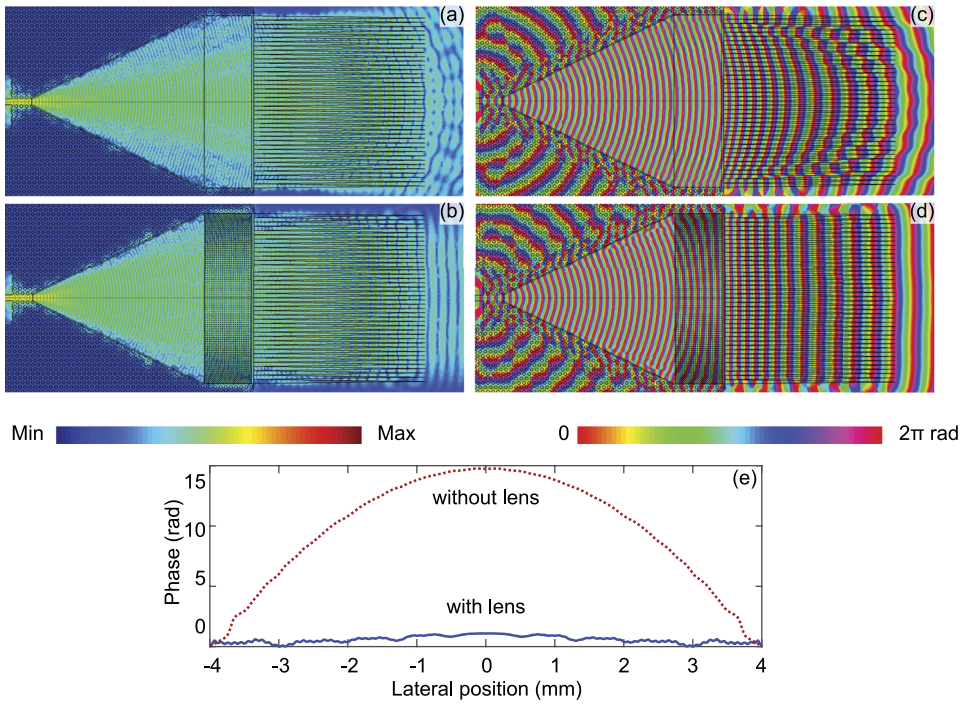

FIG. 8. Field distributions inside optimal antennas at 330 GHz. [(a) and (b)] Instantaneous amplitude of the tangential electric-field component for antennas without and with effective lens, respectively. The amplitude plots are in logarithmic scale and normalized to the same factor. [(c) and (d)] Corresponding phase distributions of the E_x component for the antennas in (a) and (b), respectively. The phase inside the photonic crystal is not meaningful due to the lack of propagation modes therein. (e) Phase profiles across the aperture of the two antennas. Note that the phase profile for the case with no lens differs from that in Fig. 4(a), as they are taken at different planes along the z axis.

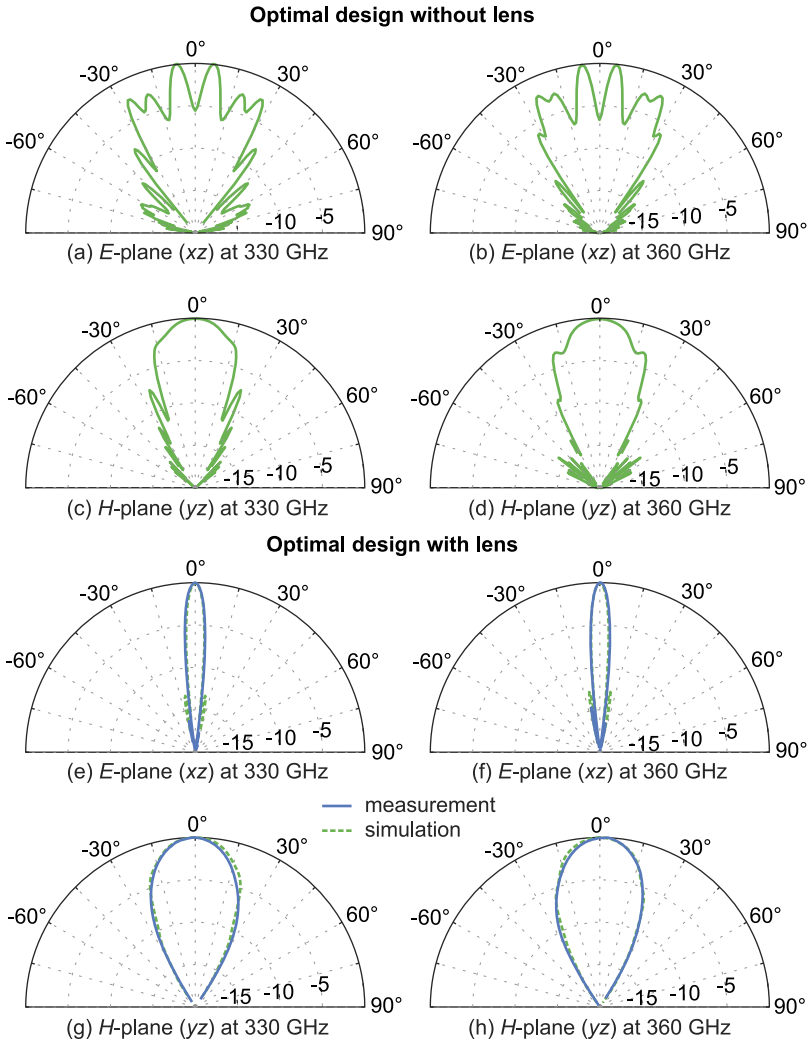

FIG. 9. Normalized radiation patterns at 330 GHz (left) and 360 GHz (right). [(a)–(d)] Simulated patterns for optimal design without effective lens. [(e)–(h)] Simulated and measured patterns for optimal design with effective lens. The measurement is with an angular resolution of 1°.

the beam width of about 11° in both planes. The sidelobe levels in the *E*- and *H*-plane are well below −10 dB and −15 dB, respectively. The lack of grating lobes in the *H*-plane implies no leakage of the mode inside the effective lens. Notably the measured patterns are nearly indistinguishable from the numerical estimations.

IV. SHORT-RANGE WIRELESS COMMUNICATIONS

This section demonstrates the use of the optimal dielectric rod antenna arrays for wireless communications. Since the antennas are broadband and directional, they can be used for point-to-point transmission with a high data rate. Figure 10 illustrates the transceiver setup for bit-error-rate (BER) testing and 4K-resolution video transmission. On the transmitter side, optical signals from two tunable near-infrared lasers are modulated by on-off keying (OOK) with Gbit/s data from either a pulse-pattern generator or a 4K video player. The modulated optical signals are then amplified by an EDFA and downconverted by a UTC-PD into the terahertz regime at the beating frequency of 343 GHz. The resulting terahertz carrier modulated with the digital data is then radiated by the rod antenna array into free space. On the receiver side, an identical rod antenna array captures the radiation and feeds into a SBD to extract the data via envelope detection. The demodulated signal is then amplified by

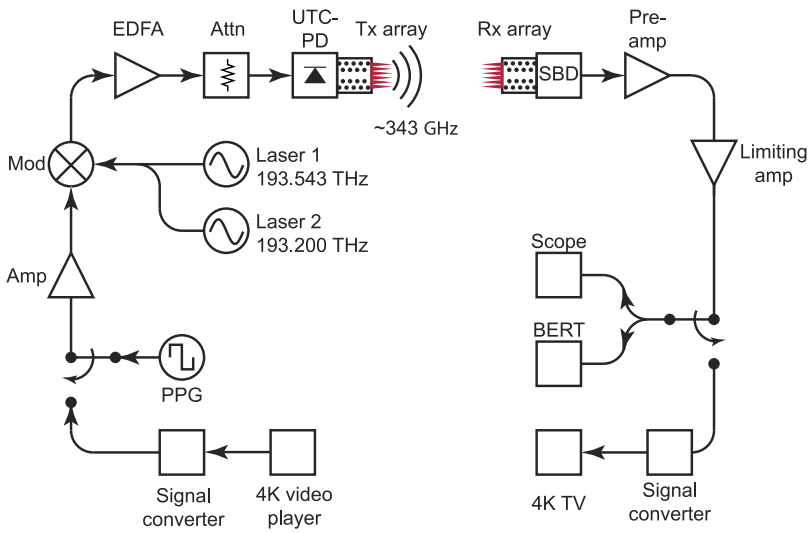

FIG. 10. Transceiver chain for short-range wireless communications. Both the bit-error-rate measurement and 4K-resolution video transmission use the same terahertz source from the beating frequency of the two near-infrared lasers. The antenna pair is fully aligned and polarization-matched. Attn: attenuator, Amp: amplifier, PPG: pulse-pattern generator, Mod: optical modulator, EDFA: erbium-doped fiber amplifier, UTC-PD: uni-travelling carrier photodiode, Tx: transmitter, Rx: receiver, SBD: Schottky barrier diode, Scope: oscilloscope, and BERT: bit-error-rate tester.

a preamplifier and reshaped by a limiting amplifier. The eye diagram and bit error rate of the transmitted signal are then measured by using an oscilloscope and a bit-error tester, respectively. For the 4K-resolution video transmission, the signal is digitally converted and displayed on a television.

The antenna pair is separated by 3 mm for transmitting and receiving 10 Gbit/s data. Figure 11(a) shows the BER as a function of the transmitted power at the UTC-PD. It is clear that error-free

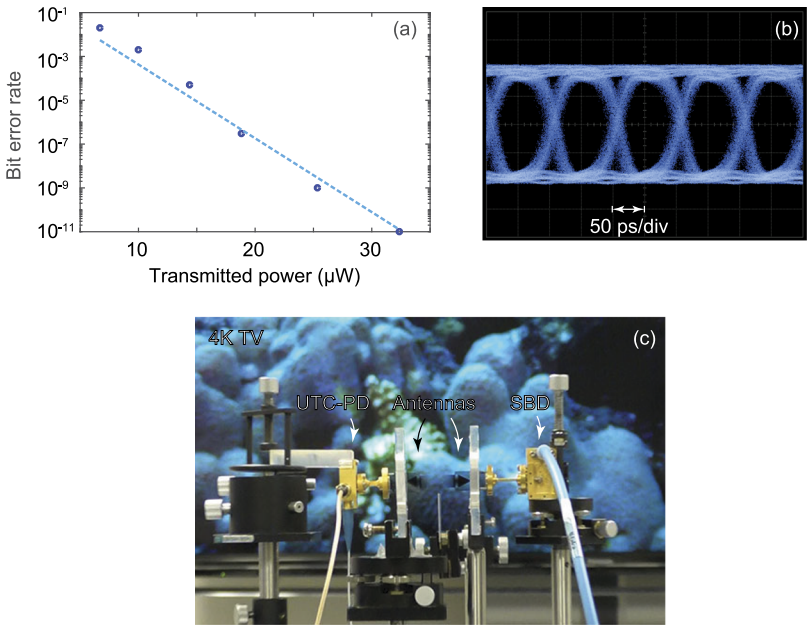

FIG. 11. Wireless communications at 343 GHz. (a) BER as a function of the transmitted power at the data rate of 10 Gbit/s. The threshold for error-free transmission is at BER = 10^{-11}. (b) Measured eye diagram at a data rate of 10 Gbit/s with error-free transmission. (c) Uncompressed 4K-resolution video at 6 Gbit/s being transmitted and received by the antenna pair (see the video file in the supplementary material).

transmission, i.e., BER < 10^{-11}, across this distance can be attained when the power is larger than 32 μW. A corresponding eye diagram in Fig. 11(b) is clearly open for the 10-Gbit/s data. This maximum data rate is limited by the output power of the UTC-PD. The antenna separation is increased to 7 mm for transmission of uncompressed 4K video signal at the bit rate of 6 Gbit/s. Figure 11(c) depicts a still image of this successful error-free video transmission (see the video file in the supplementary material). It should be noted that the transmission distance is largely limited by the available transmission power.

V. CONCLUSION

We have proposed and experimentally validated a series of dielectric rod antenna arrays fed by a photonic crystal waveguide. An all-dielectric route eliminates Ohmic loss that is accentuated by resonant metallic antennas at this frequency range. Critical to this antenna array is the use of an effective medium to equalize the phase front across a large aperture size. As a result, the optimal design attains a gain of over 20 dBi and a stable radiation pattern across the 21% bandwidth between 315 and 390 GHz, limited by the measurement system. While the gain and bandwidth performance is close to that of a standard horn antenna, this entire dielectric rod antenna array, together with the waveguide feed, is fully planar and can be fabricated onto a single silicon wafer at once. The experiments demonstrate error-free transmission at the data rate of 10 Gbit/s via OOK. This antenna implementation can potentially benefit a short distance link between multi-channel parallelly aligned transceivers and can be used for line scanning of objects. The design is readily scalable for a larger radiation gain by expanding the aperture size, and it can also be scalable to other frequency ranges. The antennas and waveguides can also be scaled to operate in other atmospheric windows within the terahertz range. However, the atmospheric attenuation, free-space path loss, and available source power will determine the transmission range, which in turn dictates possible communication applications. This design contributes to a future terahertz integrated platform on photonic crystal waveguides toward short-range communications with a high data rate.

SUPPLEMENTARY MATERIAL

See supplementary material for more details on the radiation gain profiles of additional rod antennas and the dimensions of the rod antenna arrays described in Fig. 5. The coupling between the photonic crystal waveguide and the WR-3 hollow rectangular waveguide is elaborated therein.

ACKNOWLEDGMENTS

We wish to acknowledge support from the following grants: Core Research for Evolutional Science and Technology (CREST) program, Japan Science and Technology Agency (JST) (No. JPMJCR1534); Grant-in-Aid for Scientific Research, the Ministry of Education, Culture, Sports, Science and Technology of Japan (No. 17H01064); Australian Research Council Discovery Projects (Nos. ARC DP170101922 and DP180103561). We thank Xiongbin Yu, Yuki Kimura, and Yousuke Nishida for their assistance in experiments.

[1] T. Nagatsuma, G. Ducournau, and C. C. Renaud, "Advances in terahertz communications accelerated by photonics," Nat. Photonics **10**, 371–379 (2016).
[2] P. U. Jepsen and S. R. Keiding, "Radiation patterns from lens-coupled terahertz antennas," Opt. Lett. **20**, 807 (1995).
[3] K. Okada, K. Kasagi, N. Oshima, S. Suzuki, and M. Asada, "Resonant-tunneling-diode terahertz oscillator using patch antenna integrated on slot resonator for power radiation," IEEE Trans. Terahertz Sci. Technol. **5**, 613–618 (2015).
[4] S. Diebold, S. Nakai, K. Nishio, J. Kim, K. Tsuruda, T. Mukai, M. Fujita, and T. Nagatsuma, "Modeling and simulation of terahertz resonant tunneling diode-based circuits," IEEE Trans. Terahertz Sci. Technol. **6**(5), 716–723 (2016).
[5] N. T. Yardimci, S.-H. Yang, C. W. Berry, and M. Jarrahi, "High-power terahertz generation using large-area plasmonic photoconductive emitters," IEEE Trans. Terahertz Sci. Technol. **5**, 223–229 (2015).
[6] C. Wang, B. Lu, C. Lin, Q. Chen, L. Miao, X. Deng, and J. Zhang, "0.34-THz wireless link based on high-order modulation for future wireless local area network applications," IEEE Trans. Terahertz Sci. Technol. **4**, 75–85 (2014).
[7] I. Kallfass, F. Boes, T. Messinger, J. Antes, A. Inam, U. Lewark, A. Tessmann, and R. Henneberger, "64 Gbit/s transmission over 850 m fixed wireless link at 240 GHz carrier frequency," J. Infrared, Millimeter, Terahertz Waves **36**, 221–233 (2015).
[8] T. Nagatsuma, K. Oogimoto, Y. Inubushi, and J. Hirokawa, "Practical considerations of terahertz communications for short distance applications," Nano Commun. Networks **10**, 1–12 (2016).

[9] D. Hou, W. Hong, W.-L. Goh, J. Chen, Y.-Z. Xiong, S. Hu, and M. Madihian, "D-band on-chip higher-order-mode dielectric-resonator antennas fed by half-mode cavity in CMOS technology," IEEE Trans. Antennas Propag. Mag. **56**, 80–89 (2014).
[10] X.-D. Deng, Y. Li, C. Liu, W. Wu, and Y.-Z. Xiong, "340 GHz on-chip 3-D antenna with 10 dBi gain and 80% radiation efficiency," IEEE Trans. Terahertz Sci. Technol. **5**, 619–627 (2015).
[11] W. Withayachumnankul, R. Yamada, C. Fumeaux, M. Fujita, and T. Nagatsuma, "All-dielectric integration of dielectric resonator antenna and photonic crystal waveguide," Opt. Express **25**, 14706 (2017).
[12] G. E. Mueller and W. A. Tyrrell, "Polyrod antennas," Bell Syst. Tech. J. **26**, 837–851 (1947).
[13] S. Kobayashi, R. Mittra, and R. Lampe, "Dielectric tapered rod antennas for millimeter-wave applications," IEEE Trans. Antennas Propag. **30**, 54–58 (1982).
[14] A. Patrovsky and K. Wu, "94-GHz planar dielectric rod antenna with substrate integrated image guide (SIIG) feeding," IEEE Antennas Wireless Propag. Lett. **5**, 435–437 (2006).
[15] N. Ghassemi and K. Wu, "Planar dielectric rod antenna for gigabyte chip-to-chip communication," IEEE Trans. Antennas Propag. **60**, 4924–4928 (2012).
[16] A. Rivera-Lavado, S. Preu, L. E. Garcia-Munoz, A. Generalov, J. M. de Paz, G. Dohler, D. Lioubtchenko, M. Mendez-Aller, F. Sedlmeir, M. Schneidereit, H. G. L. Schwefel, S. Malzer, D. Segovia-Vargas, and A. V. Raisanen, "Dielectric rod waveguide antenna as THz emitter for photomixing devices," IEEE Trans. Antennas Propag. **63**, 882–890 (2015).
[17] S. M. Hanham, T. S. Bird, B. F. Johnston, A. D. Hellicar, and R. A. Minasian, "A 600 GHz dielectric rod antenna," in *3rd European Conference on Antennas and Propagation (EuCAP)* (IEEE, 2009), pp. 1645–1647.
[18] A. A. Generalov, J. A. Haimakainen, D. V. Lioubtchenko, and A. V. Raisanen, "Wide band mm- and sub-mm-wave dielectric rod waveguide antenna," IEEE Trans. Terahertz Sci. Technol. **4**, 568–574 (2014).
[19] J. Pousi, D. Lioubtchenko, S. Dudorov, and A. Raisanen, "High permittivity dielectric rod waveguide as an antenna array element for millimeter waves," IEEE Trans. Antennas Propag. **58**, 714–719 (2010).
[20] R. Kazemi, A. E. Fathy, and R. A. Sadeghzadeh, "Dielectric rod antenna array with substrate integrated waveguide planar feed network for wideband applications," IEEE Trans. Antennas Propag. **60**, 1312–1319 (2012).
[21] A. Rivera-Lavado, L.-E. García-Muñoz, A. Generalov, D. Lioubtchenko, K.-A. Abdalmalak, S. Llorente-Romano, A. García-Lampérez, D. Segovia-Vargas, and A. V. Räisänen, "Design of a dielectric rod waveguide antenna array for millimeter waves," J. Infrared, Millimeter, Terahertz Waves **38**, 33–46 (2017).
[22] J. Dai, J. Zhang, W. Zhang, and D. Grischkowsky, "Terahertz time-domain spectroscopy characterization of the far-infrared absorption and index of refraction of high-resistivity, float-zone silicon," J. Opt. Soc. Am. B **21**, 1379 (2004).
[23] K. Tsuruda, M. Fujita, and T. Nagatsuma, "Extremely low-loss terahertz waveguide based on silicon photonic-crystal slab," Opt. Express **23**, 31977 (2015).
[24] Z. Wu, M. Liang, W.-R. Ng, M. Gehm, and H. Xin, "Terahertz horn antenna based on hollow-core electromagnetic crystal (EMXT) structure," IEEE Trans. Antennas Propag. **60**, 5557–5563 (2012).
[25] M. Fujita, T. Nagatsuma, T. Ishigaki, D. Onishi, and E. Miyai, "Terahertz-wave connector and terahertz-wave integrated circuits, and wave guide and antenna structure," U.S. patent 2014/0248020 (4 September 2014).
[26] S.-G. Park, K. Lee, D. Han, J. Ahn, and K.-H. Jeong, "Subwavelength silicon through-hole arrays as an all-dielectric broadband terahertz gradient index metamaterial," Appl. Phys. Lett. **105**, 091101 (2014).
[27] J. Hunt, T. Tyler, S. Dhar, Y.-J. Tsai, P. Bowen, S. Larouche, N. M. Jokerst, and D. R. Smith, "Planar, flattened Luneburg lens at infrared wavelengths," Opt. Express **20**, 1706 (2012).
[28] L. H. Gabrielli, J. Cardenas, C. B. Poitras, and M. Lipson, "Silicon nanostructure cloak operating at optical frequencies," Nat. Photonics **3**, 461–463 (2009).
[29] A. Subashiev and S. Luryi, "Modal control in semiconductor optical waveguides with uniaxially patterned layers," J. Lightwave Technol. **24**, 1513–1522 (2006).
[30] B. E. A. Saleh and M. C. Teich, *Fundamentals of Photonics*, 2nd ed. (John Wiley & Sons, Inc., 2007).